Surface Wave Measurements from Subsurface Floats

ERIC D'ASARO

Applied Physics Laboratory, and School of Oceanography, University of Washington, Seattle, Washington

(Manuscript received 16 September 2014, in final form 21 December 2014)

ABSTRACT

Pressure gradient measurements on a subsurface Lagrangian float are used to measure the spectrum of surface waves for 100 days of measurements at Ocean Weather Station *Papa*. Along Lagrangian trajectories of surface waves, the pressure is constant and the vertical pressure gradient fluctuations equal the Eulerian fluctuations at the mean float depth to second order in wave height. Measurement of the pressure difference between the top and the bottom of the float can thus be used to measure the waves. Corrections for the wave decay with depth, for the vertical motion of the float, for the finite sampling interval, and for the sampling noise (among others) are necessary to obtain accurate results. With these corrections, scalar spectra accurately match those from a nearby Waverider buoy for significant wave heights greater than about 3 m. For smaller wave heights, noise in the pressure measurements biases the float spectral measurements. Significant wave height is measured with an rms error of 0.37 m over the measured range of 1–9 m. This demonstrates that Lagrangian floats accurately follow the Lagrangian trajectories of surface waves. More detailed and quieter measurements of float motion could likely measure directional wave spectra from below the surface. Similar methods could be used to infer surface wave properties from other subsurface vehicles.

1. Introduction

Measurements at the air–sea interface are crucial for monitoring, parameterizing, and understanding the behavior of both the ocean and atmosphere. Maintaining sensors here, however, is often difficult: vibration and impact from the constant wave motion is destructive, intermittent saltwater immersion is corrosive, biological fouling is difficult to prevent, and vandalism is common. Measurements of air–sea properties using sensors away from the interface overcome many of these difficulties; satellite-based wind speed (Risien and Chelton 2008) and sea surface temperature (Reynolds et al. 2002) measurements are prominent examples. Such remote sensing of air–sea properties is also possible from beneath the surface, for example, passive acoustic measurements of wind and rain (Ma et al. 2005). The long-term arrays of floats, drifters, and gliders (see special issue of *Limnology and Oceanography,* 2008, Vol. 53, No. 5, part 2) offer many opportunities for deploying such measurements, both for large-scale monitoring and as part of localized process experiments.

Pressure variations at fixed points are commonly used to measure surface waves in shallow water. D'Asaro et al. (1996, his Fig. 4) describes estimates of the surface wave field from pressure measurements made on a subsurface float. This paper further develops this approach using a much larger dataset and tests it against standard surface wave measurements from a Waverider buoy. The novelty in this approach is that it exploits the unique properties of surface waves when measured in a Lagrangian reference frame. Measurements are made from a "Lagrangian float" (D'Asaro 2003), an approximately 1-m long, 50-L displacement cylinder with active buoyancy control that matches its density to that of seawater to an accuracy of a few grams (Fig. 1). This small residual buoyancy acting on an approximately 1-m^2 area horizontal drogue, results in a net vertical motion relative to the water of a few millimeters per second (D'Asaro et al. 2014). Accordingly, the float accurately follows the three-dimensional motion of water parcels at surface wave frequencies.

The pressure along Lagrangian trajectories due to linear, freely propagating, inviscid surface waves is constant. This is apparent at the ocean surface for a floating object; it both follows the water and remains at atmospheric pressure. Appendix A shows that pressure along Lagrangian trajectories is constant to at least

Corresponding author address: Eric D'Asaro, Applied Physics Laboratory, University of Washington, 1013 NE 40th Street, Seattle, WA 98105-6698.
E-mail: dasaro@apl.washington.edu

DOI: 10.1175/JTECH-D-14-00180.1

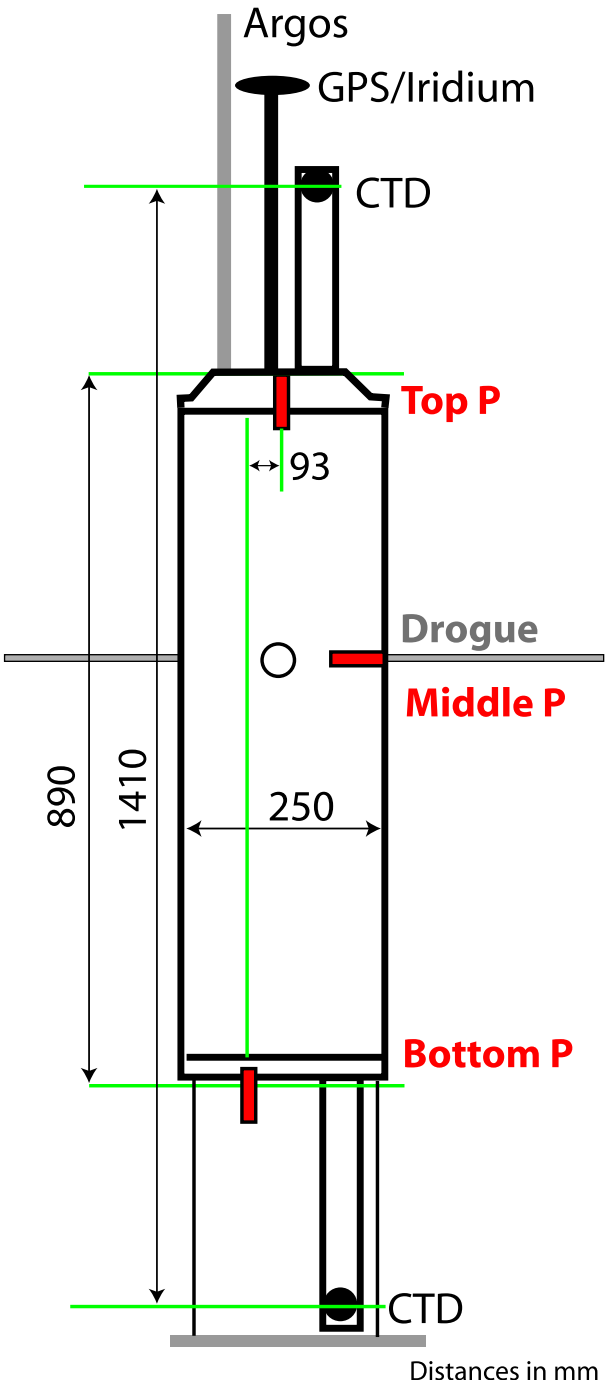

FIG. 1. The Lagrangian float used in this study. Pressure was measured at three points along the float hull (red). The top and bottom sensors are nearly aligned vertically and have the largest vertical separation, and are thus used for the analysis.

second order in wave height at all depths. The increased hydrostatic pressure beneath the wave crests is exactly balanced by the nonhydrostatic acceleration of water trajectories curving downward around the crest. A pressure sensor at the center of a perfectly Lagrangian float thus sees no signal due to surface waves, a feature that allows the float to accurately filter out the very large Eulerian pressure signals (typically equivalent to few meters) due to surface waves and thus measure the much smaller pressure changes due to its own advection by boundary layer turbulence (typically $\sim 0.01\ \mathrm{m\,s^{-1}}$).

The pressure gradient fluctuations along a Lagrangian trajectory are the same as the Eulerian fluctuations to second order (see appendix A). These fluctuations are measured using the difference between measurements from two pressure sensors, one at each end of the float (Fig. 1). In the simple case of a sinusoidal wave with surface displacement,

$$\zeta = a\cos(kx - \omega t), \tag{1}$$

where $\omega^2 = gk$ expresses the dispersion relationship between radian frequency ω and wavenumber k based on g, the acceleration of gravity. The cyclic frequency is expressed as $f = \omega/2\pi$. The vertical (z, positive upward) pressure gradient along a Lagrangian trajectory centered at position z_0 and x_0 is

$$\frac{\partial P}{\partial z} = -1 + ake^{kz_0}\cos(kx_0 - \omega t). \tag{2}$$

Pressure will be henceforth expressed in hydrostatic depth units (i.e., divided by $g\rho$, where ρ is the water density), so pressure has units of meters and the pressure gradient is dimensionless (meters per meter). The float measures pressure fluctuations using

$$P'_z = \frac{\partial P}{\partial z} + 1. \tag{3}$$

The wave amplitude is thus

$$a = \langle 2P'^2_z\rangle^{1/2} k^{-1} e^{-kz_0} \tag{4}$$

with k computed from the known frequency and the angle brackets $\langle\ \rangle$ denote a time mean, so that $\langle\cos^2(kx_0 - \omega t)\rangle = 0.5$. The surface amplitude can thus be computed from the subsurface pressure gradient fluctuations.

In practice, this calculation is complicated by a variety of experimental issues that are the focus of this paper. Some readers may wish to skip to section 3, where the results are presented.

2. Measurements

The Lagrangian float was air-deployed near Ocean Weather Station *Papa* (OWS-*P*) by the 53rd Air Force

Reserve unit, ''Hurricane Hunters,'' on 9 February 2011, was operated for 100 days, and was recovered by the Canadian Coast Guard Ship (CCGS) *John P. Tully* as part of its annual June cruise to OWS-*P*. During ''Lagrangian drifts'' occupying most of each day, the float tracked the three-dimensional motion of water parcels, actively controlling its buoyancy to match that of the mixed layer and opening a horizontal drogue to increase its vertical drag (D'Asaro et al. 1996; Harcourt and D'Asaro 2010). The float was repeatedly carried across the mixed layer by the turbulence within the layer at typical vertical speeds of $10-20\,\mathrm{mm\,s^{-1}}$. The float trajectories thus nearly uniformly fill the 20–80-m-deep mixed layer and thus repeatedly sample the upper part of the mixed layer, where the surface waves are the strongest. The same selected high-quality data segments used in D'Asaro et al. (2014) were used here.

Pressure was measured at three points along the float hull (red in Fig. 1) using Druck PDCR pressure sensors. The top and bottom sensors were nearly vertically aligned (a lateral separation of about 9 mm) and had a larger vertical separation than pairs including the middle sensor. This pair was thus used in all of the subsequent analysis. All three pressure sensors were sampled at 1 Hz using a 24-bit analog-to-digital (A/D) on a centrally located board. Analog voltage signals from each pressure sensor were transmitted down a shielded twisted pair to this board. Interference from the many other electronic systems was minimized by careful attention to additional shielding and cable location; nevertheless, such signals appear to limit the accuracy of the pressure measurements. There may be additional signals in the pressure that are associated with float motion, float tilts, or flow turbulence, but these cannot be diagnosed using the sensors on these floats. All signals that do not appear to be surface waves are thus called ''noise.'' This noise was dominated by harmonics of the main 30-s float sampling period. This signal was removed by Fourier transforming the data, replacing values within 0.0018 Hz of each harmonic with random Gaussian complex numbers with an rms amplitude matching that between 0.0018 and 0.0036 Hz of the harmonic, and inverse Fourier transforming. The remaining noise was approximately white with a level of 1–10 mm depending on the sensor.

Wave spectral data were collected at OWS-*P* using a 0.9-m Datawell directional Waverider (DWR MKIII) buoy moored in 4255-m water depth at 49.98°N, 145.09°W from 15 June 2010 until recovery on 4 October 2012. The upper portion (surface to 150-m depth) of the mooring included a 30-m rubber cord and a 3:1 scope ratio, such that the Waverider could move freely and follow the waves. The lower portion (150–4255-m depth) was tensioned by a subsurface float, such that the mooring has a small watch circle (<1000 m) despite the substantial depth of the location. The Waverider collected buoy pitch, roll, and heave displacements at 1.28 Hz on a half-hour duty cycle; energy frequency spectra $E(f)$ and spectral moments (a_1, b_1, a_2, b_2) were computed on board. The spectra were transmitted via Iridium satellite modem to the Coastal Data Information Program (CDIP) at the Scripps Institution of Oceanography, where the data are publicly available online (at http://cdip.ucsd.edu) as Station 166. The data are also posted on the National Data Buoy Center (NDBC) website (http://www.ndbc.noaa.gov) as Station 46246.

The float was deployed about 1.5 km from the Waverider. It drifted southward and westward, reaching a maximum distance of 116 km on day 104, and then moving back to reach a distance of 58 km at the end of the record (day 141).

3. Analysis

a. Simulations

The vertical motion of the float through the broadband, vertically decaying surface wave signal makes the quantitative computation of wave spectra from pressure gradient much more complicated than that in (4). The analysis methods were therefore developed using a simulated set of measurements. A model wave spectrum was defined as having a slope of ω^{-4} for $\omega > \omega_{\mathrm{peak}}$ and a value 100 times less than the peak value for $\omega < \omega_{\mathrm{peak}}$. Realizations of this spectrum were generated for a given wave variable at a specified depth and time by summing the contributions in each frequency band using the equations in the appendixes. The phase of each contribution was randomized, but the amplitude was fixed to be exactly that of the test spectrum, so that more exact comparison between the test and the computed spectra could be made. Figure 2 shows the model spectrum (red), 10 realizations of the surface displacement (blue), and the average of 300 such realizations (black). For sampling at a fixed surface point, a simple spectrum of the realizations thus reproduces the test spectrum.

Sampling by a moving float was simulated using a sinusoidal float trajectory across a mixed layer of depth H with the maximum vertical speed specified. Typical parameter values are $H = 30\,\mathrm{m}$ and $W_{\mathrm{max}} = 0.03\,\mathrm{m\,s^{-1}}$. For sampling by a real float, corrections for six different effects were found to be necessary. The analysis steps are described below in approximate order of application, simplicity, and importance.

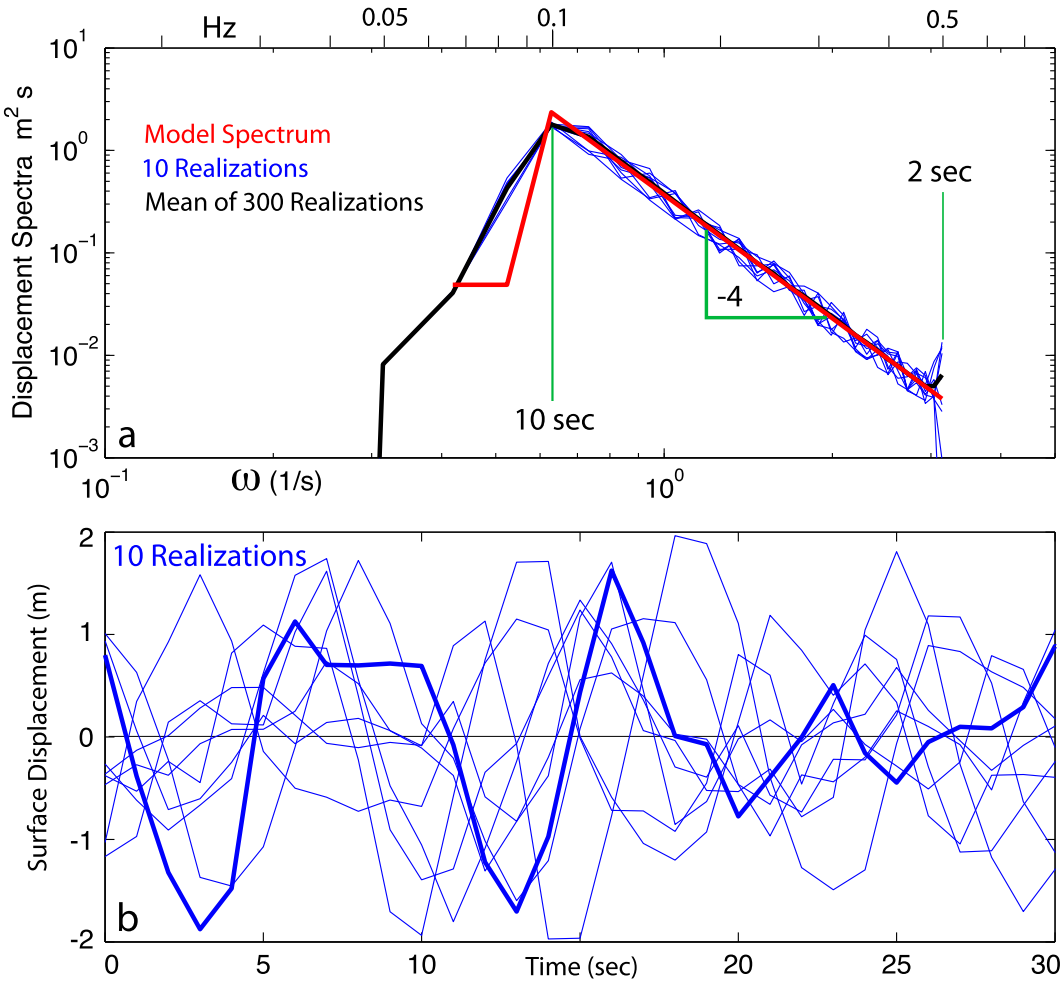

FIG. 2. (a) Test spectrum of surface waves (red) has a −4 slope up to the peak frequency. Ten realizations of the spectrum (blue) and the mean of 300 realizations (black) closely track the test spectrum above the peak. Below the peak, the test spectrum falls off more quickly than can be measured by the windowed spectra of the realizations. Realizations in this case were 600 s long. Top axis is frequency in hertz; bottom axis is frequency in radian per second. (b) Ten realizations of vertical displacement.

b. *Spectrogram*

The pressure gradient is computed as the difference between the top and bottom pressure sensors, divided by the distance between them:

$$P_z = (P_{\text{top}} - P_{\text{bottom}})/(Z_{\text{top}} - Z_{\text{bottom}}). \qquad (5)$$

Any differences between the vertical and along-float directions are ignored. The P_z time series is cleaned by removing the harmonic of 30 s as described above. This is done on long data segments ($\sim 20 \times 10^4$ s) because of the high spectral resolution necessary. Wave spectra are then taken on a large number of shorter data segments in order to minimize the float's vertical displacement during each segment. The result is a spectrogram of pressure gradient variance as a function of time t (s) and radial frequency ω (s^{-1}). The data segment length T is an important analysis parameter. Typical values of 120 s can resolve the surface wave peak frequency while minimizing the effect of float motion. The spectrogram computed directly from the measured pressure will be denoted as $\mathcal{S}^{(0)}_{P_z}$.

c. *Noise correction (NC)*

The residual measurement noise is assumed to be white. The rms noise δ_{P_z} is an important analysis parameter. A typical value is 0.01, that is, 0.01 m across the 1-m float. This variance, spread out uniformly across the spectral bandwidth, is subtracted from the computed spectra:

$$\mathcal{S}^{(1)}_{P_z} = \mathcal{S}^{(0)}_{P_z} - (\delta_{P_z})^2 \frac{\pi}{\delta t}. \qquad (6)$$

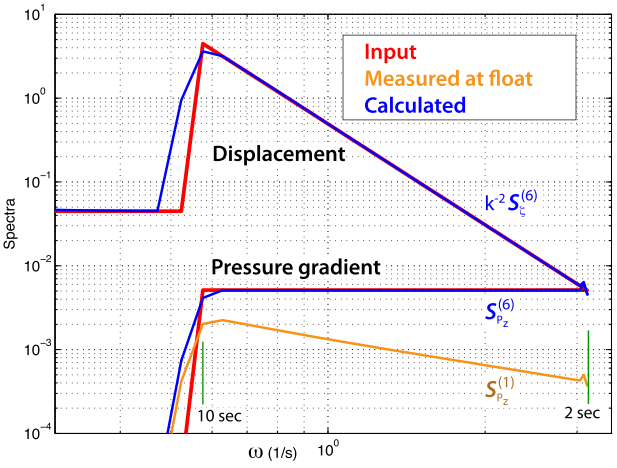

FIG. 3. Simulated measurement of surface wave spectra. Input spectra of displacement at the surface (top red) and pressure gradient at the surface (bottom red). Pressure gradient spectrum (orange) at a float with a sinusoidal trajectory spanning a depth of 30 m and a maximum vertical velocity of 0.03 m s^{-1}. Pressure gradient at the surface calculated using all six corrections (bottom blue). Displacement at the surface calculated from pressure gradient (top blue). The input spectra of 300 realizations are averaged. Significant wave height is 2 m.

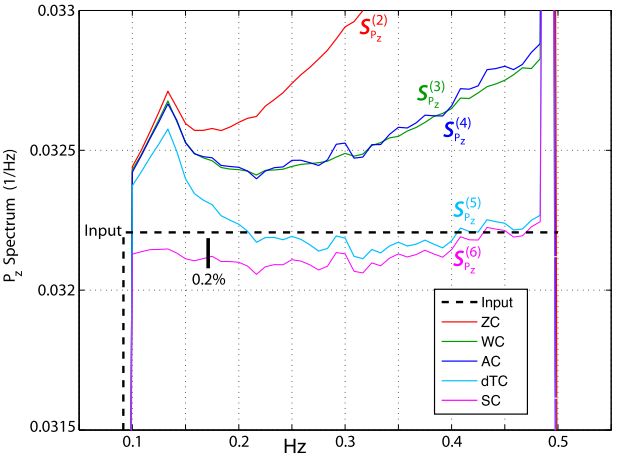

FIG. 4. Calculation of surface wave pressure gradient spectrum from measured spectrum. Figure 3 shows input spectrum and measured spectrum. Here, the cumulative effects of the depth-correction (ZC, red, $\mathcal{S}_{P_z}^{(2)}$), vertical velocity correction (WC, blue, $\mathcal{S}_{P_z}^{(3)}$), removal of large accelerations (AC, green, $\mathcal{S}_{P_z}^{(4)}$), sampling rate correction (dTC, cyan, $\mathcal{S}_{P_z}^{(5)}$), and spectral bandwidth correction (SC, magenta, $\mathcal{S}_{P_z}^{(6)}$) are shown. The final spectrum (magenta) deviates from the input spectrum by about 0.2%.

d. Depth correction (ZC)

Each spectrogram value is converted to a surface value assuming an exponential decay at a wavenumber computed from the dispersion relationship at the central frequency of the frequency bin:

$$\mathcal{S}_{P_z}^{(2)} = \mathcal{S}_{P_z}^{(1)} e^{2kZ}, \tag{7}$$

where Z is the pressure (depth) at the center of the float at the center of the time interval for each spectrogram value. Thus, in Fig. 3, the pressure gradient measured at the float (orange) is much less than that at the surface (blue or red, bottom). The effect is largest for waves with the largest k, that is, the highest frequencies. For a 2-Hz wave, $1/k \approx 1$ m, the spectrum decays by a factor of 10^6 in 7 m, so that measurements at more than a few meters below the surface are entirely due to instrumental noise. The application of (7) for such waves only amplifies noise, leading to unrealistically large spectral values. Accordingly, values of $\mathcal{S}_{P_z}^{(2)}$ with $e^{2kZ} > C_{\max}$ are flagged as bad. An important analysis parameter is $C_{\max}$; a typical value is 10. High-frequency waves can thus only be measured when the float is near the surface; lower-frequency waves can be measured over a wider range of depths.

The ZC correction typically brings $\mathcal{S}_{P_z}^{(2)}$ to within a few percent of the correct value. The correction is most accurate for the lower-frequency waves where it is smallest and largest at higher frequencies (Fig. 4, red). Additional corrections compensate for the effects of the float motion, of the finite sampling interval, and of spectral spreading due to the spectral windowing.

e. Vertical motion correction (WC)

A float with vertical velocity W moves a distance WT during a single spectrogram window. The wave amplitude changes by e^{kWT} in this distance. If kWT is large, the wave signal is much larger at the start of the interval than at the end (see Fig. 5), so that the average is biased high. Appendix B analyzes this case for a constant W and derives highly accurate corrections for both rectangular and Hanning windows, which depend only on the value of kWT. The effect is strongest for higher-frequency waves; the WC correction thus significantly reduces the high-frequency bias (Fig. 4, green). The $\mathcal{S}_{P_z}^{(2)}$ spectrogram corrected by WC is denoted as $\mathcal{S}_{P_z}^{(3)}$.

f. Acceleration editing (AC)

The value of W is computed from the centered difference of float pressure averaged over each spectrogram window. The average acceleration A is similarly computed from the difference of W. If the fractional change in W over the window (i.e., AT/W) is larger than $E_{\max}$, the spectrogram value is flagged as bad. A typical value is $E_{\max} = 0.5$. In Fig. 4 (blue) the effect is not large even at the highest frequencies. The $\mathcal{S}_{P_z}^{(3)}$ spectrogram edited for acceleration is denoted as $\mathcal{S}_{P_z}^{(4)}$.

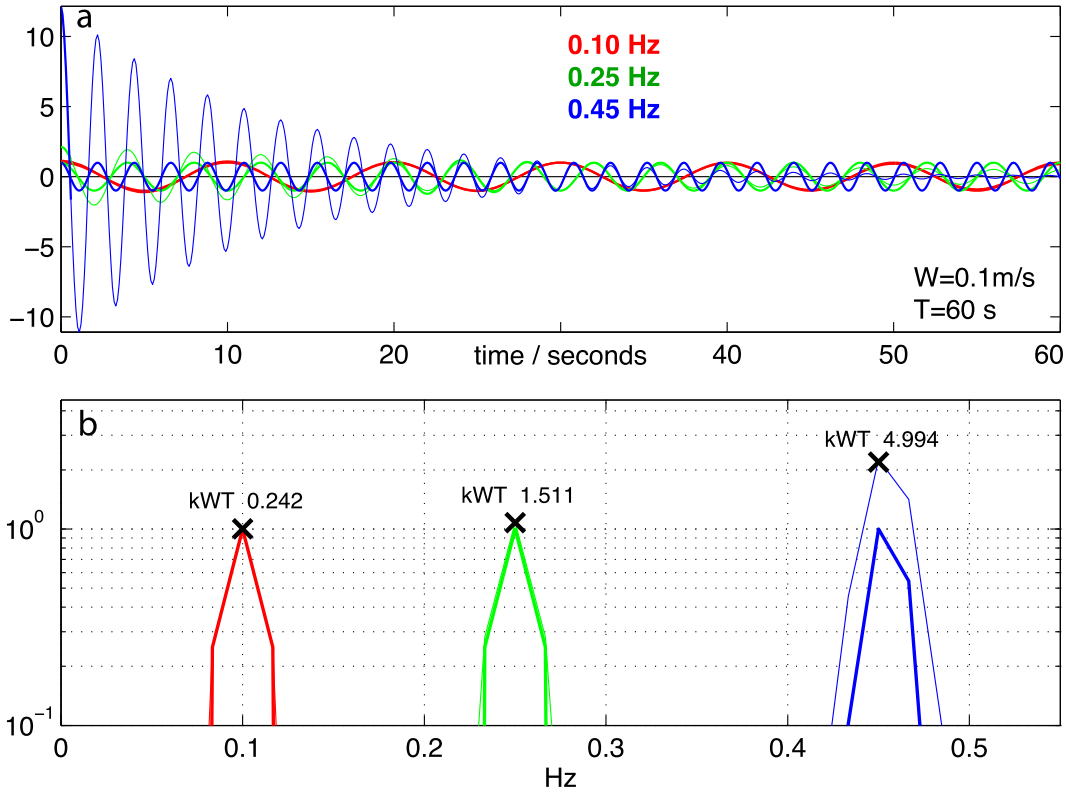

FIG. 5. (a) Simulated time series of surface wave displacement measured at a fixed depth (thick lines) and from a float descending at 0.1 m s^{-1} (thin lines) at three different wave frequencies (colors). The wave amplitude decays as the float descends. (b) Spectra for these time series for a data length of $T = 60$ s computed using a Hanning window. WC correction indicated by black crosses; values of kWT are noted for each spectrum.

g. *Sampling interval correction (dTC)*

The WC correction is derived assuming continuous sampling. In this case WC is highly accurate (Fig. 6, red). However, for a realistic sampling interval dt, it is not (Fig. 6, colors). For fixed dt and T, we assume that the additional correction depends only on kWT; we numerically simulate the effect and fit it with a quadratic polynomial (Fig. 6). Over the range of resolved wave frequencies (1/2–1/15 Hz) and expected vertical velocities (0.001–0.2 m s^{-1}), this predicts the simulated dTC correction to much better than 1% (Fig. 6). Applying this to the simulations (Fig. 4, cyan) removes almost all of the remaining high-frequency bias in the WC correction. The spectrogram $\mathcal{S}_{P_z}^{(4)}$ corrected by dTC is denoted as $\mathcal{S}_{P_z}^{(5)}$.

h. *Spectral spreading correction (SC)*

A Hanning window spreads energy at ω_0 to sidebands at $\omega_\pm = \omega_0 \pm 2\pi T^{-1}$. The two sidebands decay with different vertical scales and thereby modify the ZC correction. Appendix C derives a correction for this effect. It is largest at low frequencies because the relative spectral spreading is largest here. Applying this to the simulations (Fig. 4, magenta) removes the low-frequency peak, resulting in a nearly flat spectrum. The spectrogram $\mathcal{S}_{P_z}^{(5)}$ corrected by SC is denoted as $\mathcal{S}_{P_z}^{(6)}$.

i. *Results*

These simulations show that measuring surface waves from a vertically moving platform is much more complicated than measuring from a fixed platform. The analysis finds and corrects for six different sources of error; there are certainly more. Nevertheless, for the cases considered the fully corrected spectrum, $\mathcal{S}_{P_z}^{(6)}$, reproduces the input spectrum to about 0.2%, except in a narrow band near the Nyquist frequency.

4. Application to OWS-*P* data

The methods developed in section 3 are applied to the OWS-*P* data described in section 2. Float data were cleaned as described in section 2. Values of $\delta_{P_z} = 0.013$, $C_{\max} = 10$ and $E_{\max} = 0.5$ were used in the NC, ZC and AC corrections, respectively.

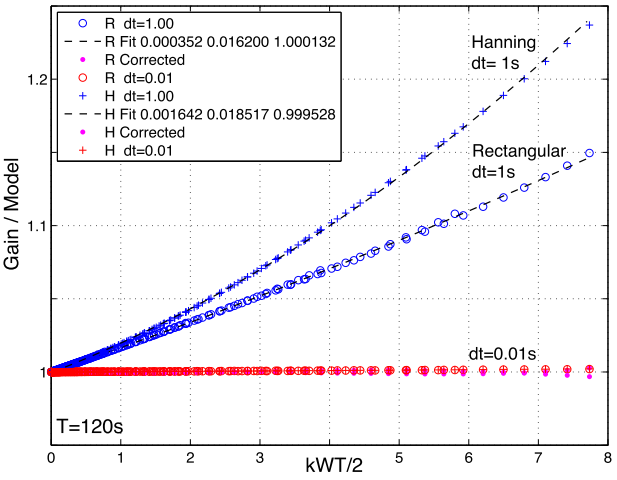

FIG. 6. Numerical simulation of WC and dTC corrections for rectangular (R in legend) and Hanning (H in legend) windows. Analyses similar to that in Fig. 5 are done for waves from 1/15 to 0.45 Hz and vertical velocities from 0.001 to 0.2 m s^{-1} to yield a wide range of kWT values (horizontal axis). For each, the vertical axis plots the ratio of spectral value to that analytically computed for the WC correction. For nearly continuous sampling (red, dt = 0.01 s), WC is nearly perfect. For dt = 1 s, the result depends on the window and is fit by a quadratic polynomial (black dashed line). When this is removed (magenta), the fit is much better than 1%. This defines the dTC correction.

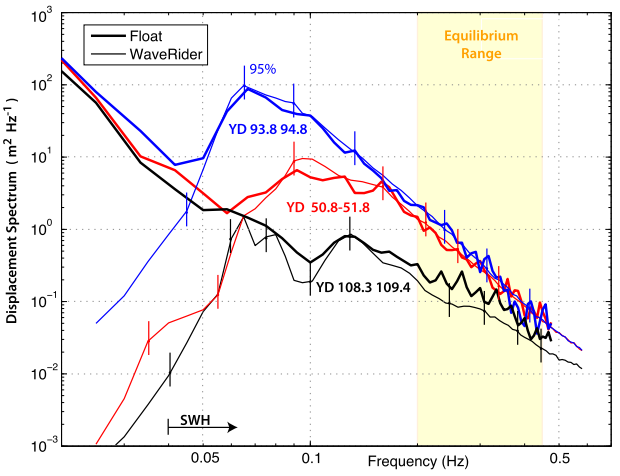

FIG. 7. Three representative displacement spectra from the OWS-*P* data. Float spectra (thick lines) are compared to Waverider spectra (thin lines). Selected 95% confidence limits for the Waverider spectra are shown. Time windows for each spectrum are noted. Yellow shading denotes the band used for computing the amplitude of the equilibrium range. Horizontal arrow shows the lower-frequency limit for computation of significant wave height.

a. *Sample spectra*

Figure 7 shows three sample spectra selected for variable energy levels and the peak wave period. The most energetic spectrum (blue) has a significant wave height of ≈9 m, the highest of the record. The float and Waverider spectra agree to within the 95% confidence limits of the Waverider spectra down to a frequency of 0.05 Hz. At lower frequencies, the float spectra rise far above the Waverider spectra, presumably due to the much higher noise in the float data.

The least energetic spectrum (black) has a significant wave height of ≈1.2 m, close to the lowest of the record. The float spectrum is roughly 50% above the Waverider spectrum out to about 0.07 Hz. The two peaks in the Waverider spectrum are resolved in the float data. At lower frequencies, the float noise again dominates. The difference between the two spectra can be reduced significantly by modest changes in the value of the float noise δ_{P_z}; adding slight frequency dependences to the noise can lead to an even better fit. It is thus clear that this spectrum is close to the noise level of the method.

The intermediate spectrum (red) has a significant wave height of ≈2.2 m. The spectral level at high frequency nearly matches that of the energetic case. The float and the Waverider spectra agree well, and both show a slightly flatter slope than for the energetic case. Both also show a broad spectral peak near 0.12 Hz. At lower frequencies, the float noise again dominates.

b. *Statistical comparisons*

Significant wave height H_s is computed from the integrated displacement variance above 0.04 Hz with spectral values below the noise set to zero. The noise level in the spectrum is computed from the mean spectral value in the first four spectral bins; this yields only a slight improvement from using the fixed δ_{P_z}. Zeroing the negative spectral values similarly yields only a slight improvement over allowing negative values. Spectra that do not extend to at least 0.3 Hz (due to filtering by $E_{\max}$ or $C_{\max}$) are discarded.

The resulting H_s (Figs. 8a,b) is well correlated with the Waverider values (r = 0.96) with an rms error of 0.37 m. The float data are gappy because the float is not always close enough to the surface to measure the high-frequency waves. Some of the difference between the float and Waverider data is probably due to their spatial separation. This is especially apparent for the maximum in wave height near day 95. At this time, the separation is close to a maximum. The peak at the Waverider occurs several hours before that at the float, resulting in a counterclockwise (green) loop in Fig. 8b at the highest energies.

The level of the equilibrium spectral range emphasizes the high-frequency waves. At frequencies above

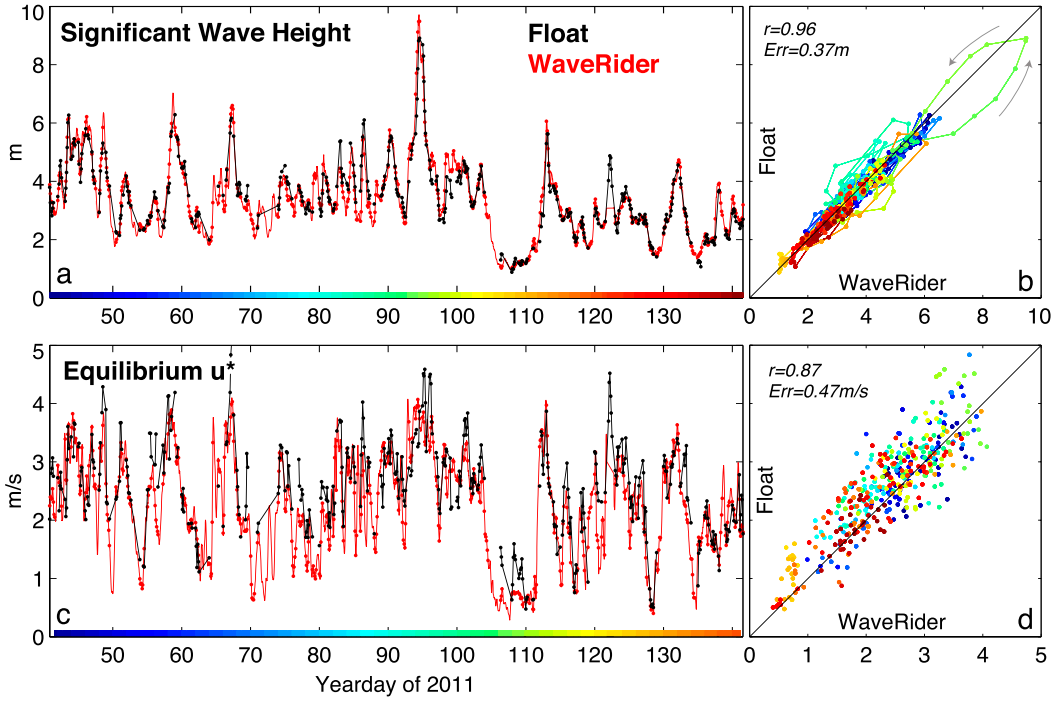

FIG. 8. Comparison of float and Waverider spectral levels. (a) Significant wave height from float (black) and Waverider (red). Colored line indicates time. (b) Scatterplot of significant wave height, float against Waverider, colored by time. Colored line shows temporal trajectory. (c) Level of equilibrium spectrum quantified by wind friction velocity u_*, colored as in (a). (d) Scatterplot of u_* as in (b).

the wave peak, scalar wave spectra commonly have a -4 slope (Toba 1973); Phillips (1985) provided a dynamical justification and an analytical expression,

$$E(\omega) = u_* 4\beta I(p) g \omega^{-4}, \tag{8}$$

where β is a constant, $I(p)$ is a directional spreading function, and u_* is the wind friction velocity. Thomson et al. (2013) analyzed the equilibrium range for this dataset using moored data at OWS-*P* to estimate u_* and found (8) to provide an accurate measure of u_* at all but the highest wind speeds using $\beta = 0.012$ and $I(p) = 2.5$. Here, we repeat this analysis and compare the u_* values obtained from the Waverider and float. The value of $u_* = \langle E\omega^4 \rangle / 4g\beta I(p)$ was computed with an average ($\langle\ \rangle$) taken over the frequency range of 0.15–0.45 Hz. Spectra with good data in less than 80% of this interval were discarded.

The resulting estimates of u_* (Figs. 8c,d) are noisier than those of wave height but are correlated with the Waverider values ($r = 0.87$) with an rms error of 0.47 m s^{-1}. Most of the low values of u_* measured by the Waverider do not have valid float values; the rejected float values are not well correlated with the Waverider values.

5. Discussion and summary

The main result of this analysis is that surface waves can be measured from a moving subsurface float by compensating for a variety of effects due to the float's depth and motion. There are two key effects. First, if the float is at depth Z, it cannot measure waves with large values of kZ, as they are strongly attenuated. However, if the float samples from a wide range of depths and the wave spectrum is assumed to be homogeneous in time, then a full spectrum can be constructed from the float data segments at various depths. For a water-following float, the ability to do this is degraded as the mixed layer deepens, because the float spends an increasingly smaller fraction of time near the surface. Second, if the float is moving vertically with speed W, the measured wave amplitude is not constant; this introduces a bias that depends on the nondimensional parameter kWT, the amount of wave decay during the sampling period T. Large values of kWT result in large corrections, since the wave decays more within T. For sufficiently large values, the wave amplitude is small for most of T and, in the presence of noise, cannot be measured. Much of this paper is concerned with the details of correcting for this effect.

Qualitatively, it introduces an intrinsic trade-off between vertical velocity and spectral resolution. If the float is moving more rapidly, a smaller value of T is required; this reduces the spectral resolution $1/T$. For sufficiently large vertical velocities, a spectrum cannot be measured. The OWS-*P* data analyzed here span a large fraction of the oceanic range of wind, waves, and mixed layer depths. Useful spectra were obtained during the entire record.

The floats used here measured the waves from the pressure gradient along the floats. This was convenient, since the wave measurements could also provide redundancy for an operationally crucial measurement. However, for wave measurements, the pressure sensors were operating at the limits of their accuracy and were thus quite noisy. Furthermore, the nonhydrostatic vertical pressure gradient is the quantity that causes vertical accelerations ($\rho w_t = -P_z$) and thus measures the same quantity as a one-axis accelerometer. It is likely that a high-quality accelerometer would provide a lower noise and easier measurement. More importantly, the success of this method implies that Lagrangian floats accurately follow surface waves' orbital motions in three dimensions. Accordingly, floats equipped with a motion package with a full 9 degrees of freedom (acceleration, rotation, and magnetometer) should be able to make better measurements of surface waves than the measurements presented here, both by distinguishing between vertical and along-float directions and by measuring the full wave directional spectra; the same corrections used here will apply to the other components of acceleration.

Although this paper addressed the ability of water-following floats to measure surface waves, similar methods should apply to measurements on other subsurface moving platforms, such as gliders and profiling floats. Their subsurface accelerations will follow surface wave trajectories in a manner similar to that of Lagrangian floats, perhaps more closely than their motions when surfaced. Pressure and/or acceleration measurements on such platforms could provide ground truth for satellite-based measurements and operational wave models.

Acknowledgments. This work was supported by the National Science Foundation (OCE0850551). We are grateful to the people and aircraft of the 53rd Air Force Reserve squadron, ''Hurricane Hunters,'' for float deployment and to the CCGS *John P. Tully* for recovery. None of this work could be possible without the excellent technical assistance of the Ocean Engineering Department at APL-UW, especially Mike Ohmart and Mike Kenney.

APPENDIX A

Wave Properties in a Lagrangian Frame

a. Basic equations

We follow Phillips (1977, section 3.2) and specify a deep-water surface wave by its surface displacements (Phillips 1977, section 3.2.1),

$$\zeta = a\cos(kx - \omega t), \tag{A1}$$

with $\omega^2 = gk$, where g is gravity. The velocity potential (Phillips 1977, section 3.2.4) is

$$\phi = a\frac{\omega}{k}e^{kz}\sin(kx - \omega t), \tag{A2}$$

where z is the vertical coordinate and positive up. Velocity $\mathbf{u} = \nabla\phi$ (Phillips 1977, section 2.4.19), so

$$u = a\omega e^{kz}\cos(kx - \omega t), \tag{A3}$$

$$w = a\omega e^{kz}\sin(kx - \omega t), \tag{A4}$$

and accelerations are

$$a_x = \frac{\partial u}{\partial t} = a\omega^2 e^{kz}\sin(kx - \omega t), \tag{A5}$$

$$a_z = \frac{\partial w}{\partial t} = -a\omega^2 e^{kz}\cos(kx - \omega t). \tag{A6}$$

A consistency check is that (A6) is $\partial^2/\partial t^2$ of (1).

Pressure, in hydrostatic depth units of $g\rho$, is given by (Phillips 1977)

$$P = -z - g^{-1}\frac{\partial\phi}{\partial t} = -z + ae^{kz}\cos(kx - \omega t). \tag{A7}$$

b. Lagrangian pressure

The first-order displacements of particles from initial positions x_0 and z_0 are

$$\chi_0 = \int_0^t u(\mathbf{x}_0, t)\,dt = -ae^{kz}\sin(kx - \omega t), \tag{A8}$$

$$\xi_0 = \int_0^t w(\mathbf{x}_0, t)\,dt = ae^{kz}\cos(kx - \omega t), \tag{A9}$$

where comparison of (A9) and (A1) provides another consistency check. The pressure at this location is

$$P(x_0 + \chi, z_0 + \xi) = P(x_0, z_0) + \frac{\partial P}{\partial x}(x_0, z_0)\chi + \frac{\partial P}{\partial z}(x_0, z_0)\xi. \tag{A10}$$

Evaluating the gradients gives

$$\frac{\partial P}{\partial x} = -ake^{kz}\sin(kx-\omega t), \tag{A11}$$

$$\frac{\partial P}{\partial z} = -1 + ake^{kz}\cos(kx-\omega t). \tag{A12}$$

A consistency check is that $a_x = -g\partial P/\partial x$. Substituting these into (A10),

$$P(x_0+\chi, z_0+\xi) = -z_0 + a^2 k e^{-2kz_0} \tag{A13}$$

with no fluctuating component to first or second order, and a second-order mean pressure gradient. The second-order pressure is similar to the mean Eulerian wave–induced pressure $-(1/2)a^2ke^{2kz_0}$ (Phillips 1977, section 3.2.17), but of twice the magnitude and of opposite sign.

c. *Lagrangian pressure gradients*

Eulerian pressure gradients are given by (A11) and (A12). Lagrangian gradients are obtained by an expansion similar to (A10),

$$\frac{\partial P}{\partial x}(x_0+\chi, z_0+\xi) = \frac{\partial P}{\partial x}(x_0,z_0) + \frac{\partial^2 P}{\partial x^2}(x_0,z_0)\chi + \frac{\partial P^2}{\partial z\partial x}(x_0,z_0)\xi, \tag{A14}$$

$$\frac{\partial P}{\partial z}(x_0+\chi, z_0+\xi) = \frac{\partial P}{\partial z}(x_0,z_0) + \frac{\partial^2 P}{\partial x\partial z}(x_0,z_0)\chi + \frac{\partial P^2}{\partial z^2}(x_0,z_0)\xi. \tag{A15}$$

Evaluating the second derivatives,

$$\frac{\partial^2 P}{\partial x^2}(x_0,z_0) = -ak^2e^{kz}\cos(kx-\omega t), \tag{A16}$$

$$\frac{\partial^2 P}{\partial z^2}(x_0,z_0) = ak^2e^{kz}\cos(kx-\omega t), \tag{A17}$$

$$\frac{\partial^2 P}{\partial z\partial x}(x_0,z_0) = -ak^2e^{kz}\sin(kx-\omega t), \tag{A18}$$

and substituting them into (A14) and (A15) produces

$$\frac{\partial P}{\partial x}(x_0+\chi, z_0+\xi) = -ake^{kz_0}\sin(kx_0-\omega t), \tag{A19}$$

$$\frac{\partial P}{\partial z}(x_0+\chi, z_0+\xi) = -1 + ake^{kz_0}\cos(kx_0-\omega t) + a^2k^2e^{2kz_0}. \tag{A20}$$

The fluctuating Lagrangian pressure gradients are the same as the Eulerian ones to second order. At second order there is an additional mean vertical gradient as in (A14).

d. *Summary*

Along a Lagrangian trajectory of a single surface wave to second order:

(i) there are no pressure fluctuations; thus, a float filters surface waves accurately.
(ii) the pressure gradient is the same as the Eulerian gradient; thus, a float can measure the surface waves from this gradient.
(iii) a vertical pressure gradient proportional to wave slope squared appears, of twice the magnitude and of opposite sign of the mean wave-induced pressure gradient; thus, a float will see a pressure and pressure gradient associated with a changing wave amplitude.

APPENDIX B

Wave Measurement Bias Due to Slow Vertical Motion

a. *The problem*

Consider measurement of a wave property P along a Lagrangian trajectory $z = Wt$ moving vertically at a constant speed W,

$$\zeta = a\sin(kx-\omega_0 t)e^{kWt}. \tag{B1}$$

Using complex notation at $x = 0$,

$$\zeta(t) = \tilde{\zeta}e^{-i\omega_0 t + kWt}. \tag{B2}$$

With $W = 0$, $\tilde{\zeta}$ can be exactly extracted from $\zeta(t)$ using a Fourier integral over an interval T. All frequencies are assumed to be multiples of the lowest resolved frequency, as for the output of an FFT,

$$\omega = \frac{2\pi}{T}n,$$
$$\omega_0 = \frac{2\pi}{T}n_0. \tag{B3}$$

With these assumptions

$$\hat{\zeta}(\omega) = \frac{1}{T}\int_{-T/2}^{T/2}\tilde{\zeta}e^{-i\omega_0 t}e^{i\omega t}\,dt = \tilde{\zeta}\delta_{nn_0}, \tag{B4}$$

returning the amplitude of the wave for $\omega = \omega_0$ and zero otherwise. However, with finite W, the wave is no longer sinusoidal. Simulating this in Fig. 6 shows the spectral

height increasing because of the exponential decay. We wish to analyze this and derive a formula to compensate for it.

b. No spectral window

We apply the same Fourier integral as in (B4) for finite W,

$$\hat{\zeta}(\omega) = \frac{1}{T}\int_{T/2}^{T/2} \tilde{\zeta} e^{-i(\omega_0-\omega)t+kWt}\, dt = \frac{1}{\Gamma}\int_{-\Gamma/2}^{\Gamma/2} \tilde{\zeta} e^{-i\delta\tau+\varepsilon\tau}\, d\tau, \tag{B5}$$

where $\tau = \omega_0 t$, $\Gamma = \omega_0 T$, $\delta = (\omega_0 - \omega)/\omega_0$, and $\varepsilon = kW/\omega_0$. Evaluating this, noting from (B4) that $e^{i\delta\Gamma/2} = e^{i\pi m} = \pm 1$ for some integer m, we find the gain G of the Fourier integral—that is, the ratio of output to input spectral level—is

$$G = \left|\frac{\hat{\zeta}}{\tilde{\zeta}}\right|^2 = \frac{\varepsilon^2}{\varepsilon^2+\delta^2}\,\frac{\sinh^2(\varepsilon\Gamma/2)}{(\varepsilon\Gamma/2)^2}. \tag{B6}$$

For $\delta \ll \varepsilon$ the spectral shape is unchanged, with gain

$$G = \left|\frac{\hat{\zeta}}{\tilde{\zeta}}\right|^2 = \left[\frac{\sinh(\varepsilon\Gamma/2)}{(\varepsilon\Gamma/2)}\right]^2 \tag{B7}$$

dependent only on $\varepsilon\Gamma = kWT$. Numerical simulations show that (B7) works exactly over many orders of magnitude.

c. Spectral window

The results change dramatically if a spectral window is added to the Fourier integral, as is usually done. Evaluating (B5) with $\delta = 0$,

$$\hat{\zeta} = \frac{\tilde{\zeta}}{\Gamma}\int_{-\Gamma/2}^{\Gamma/2} e^{\varepsilon\tau} W\left(\frac{2\pi\tau}{\Gamma}\right) d\tau, \tag{B8}$$

where $W(x)$ is the spectral window, symmetric about zero and with zeros at $x = \pm\pi$. An example is the Hanning window, where

$$W_H = h\cos^2(x/2) \tag{B9}$$

with normalization h. Changing to

$$x = \frac{2\pi\tau}{\Gamma} = 2\pi\frac{t}{T}, \tag{B10}$$

the integral is now

$$\hat{\zeta} = \frac{\tilde{\zeta}}{2\pi}\int_{-\pi}^{\pi} e^{(\varepsilon\Gamma/2\pi)x} W(x)\, dx, \tag{B11}$$

which for an arbitrary window is only a function of $\varepsilon\Gamma$. Evaluating this using the Hanning window with $h = 2$ yields

$$\hat{\zeta} = \tilde{\zeta}\frac{\pi^2}{(\varepsilon\Gamma/2)^2+\pi^2}\,\frac{\sinh(\varepsilon\Gamma/2)}{\varepsilon\Gamma/2}, \tag{B12}$$

a clear extension of (B7). This expression [(B12)] predicts gain for a Hanning window to high accuracy in numerical simulations.

d. Summary

(i) Sampling a wave at a point moving vertically at speed W can significantly bias the amplitude of the measured wave if the distance moved during a sampling interval T is comparable to the wavelength $2\pi/k$. The relevant nondimensional parameter is kWT.
(ii) The answer is also affected by the FFT window used. For an arbitrary window, the bias is a function only of kWT.
(iii) Expressions (B7) and (B12) describe the response for rectangular and Hanning windows, respectively.
(iv) These results may not apply for windows that vary rapidly.

APPENDIX C

Wave Depth Correction with Spectral Spreading

The exponential depth correction required to translate wave amplitude measured at depth Z to the surface is

$$C_0 = e^{k_0 Z} \tag{C1}$$

for a wave with frequency $\omega_0^2 = gk_0$. This can be large, a factor of 20 for $k = 1\,\mathrm{m}^{-1}$ and $Z = 3\,\mathrm{m}$, and thus amplify small errors in k_0. Because we are using a time window T, energy is spread over a band of approximately $\omega_\pm = \omega_0 \pm \delta\omega$, where $\delta\omega = 2\pi/T$. This is particularly simple for a Hanning window. Energy is spread from ω_0 to exactly $\omega_\pm$ with an amplitude of h_H, nominally 0.25, but often differing slightly depending on the details of the window implementation. Applying (C1) naively to a wave spectrum computed with a Hanning window results in a correction factor,

$$C = (1-2h_H)e^{k_0 Z} + h_H(e^{k_+ Z} + e^{k_- Z}), \tag{C2}$$

where $\omega_{\pm}^2 = gk_{\pm}$, which differs from the nominal one by a factor,

$$\frac{C}{C_0} = 1 + 2h_H[\cosh(\delta kZ) - 1], \tag{C3}$$

where

$$\delta k = k_{\pm} - k_0 = [(\omega_0 + \delta\omega)^2 - \omega_0^2]/g, \tag{C4}$$

which could be simplified but with little gain. The spectral spreading thus increases the correction factor for finite Z and $\delta\omega$, resulting in an overestimate of the computed surface wave amplitude. This bias can be corrected using (C3).

REFERENCES

D'Asaro, E. A., 2003: Performance of autonomous Lagrangian floats. *J. Atmos. Oceanic Technol.,* **20,** 896–911, doi:10.1175/1520-0426(2003)020<0896:POALF>2.0.CO;2.

——, D. M. Farmer, J. T. Osse, and G. T. Dairiki, 1996: A Lagrangian float. *J. Atmos. Oceanic Technol.,* **13,** 1230–1246, doi:10.1175/1520-0426(1996)013<1230:ALF>2.0.CO;2.

——, J. Thomson, A. Y. Shcherbina, R. R. Harcourt, M. F. Cronin, M. A. Hemer, and B. Fox-Kemper, 2014: Quantifying upper ocean turbulence driven by surface waves. *Geophys. Res. Lett.,* **41,** 102–107, doi:10.1002/2013GL058193.

Harcourt, R. R., and E. A. D'Asaro, 2010: Measurement of vertical kinetic energy and vertical velocity skewness in oceanic boundary layers by imperfectly Lagrangian floats. *J. Atmos. Oceanic Technol.,* **27,** 1918–1935, doi:10.1175/2010JTECHO731.1.

Ma, B. B., J. A. Nystuen, and R.-C. Lien, 2005: Prediction of underwater sound levels from rain and wind. *J. Acoust. Soc. Amer.,* **117,** 3555–3565, doi:10.1121/1.1910283.

Phillips, O. M., 1977: *The Dynamics of the Upper Ocean.* 2nd ed. Cambridge University Press, 344 pp.

——, 1985: Spectral and statistical properties of the equilibrium range in wind-generated gravity waves. *J. Fluid Mech.,* **156,** 505–531, doi:10.1017/S0022112085002221.

Reynolds, R. W., N. A. Rayner, T. M. Smith, D. C. Stokes, and W. Wang, 2002: An improved in situ and satellite SST analysis for climate. *J. Climate,* **15,** 1609–1625, doi:10.1175/1520-0442(2002)015<1609:AIISAS>2.0.CO;2.

Risien, C., and D. Chelton, 2008: A global climatology of surface wind and wind stress fields from eight years of QuikSCAT scatterometer data. *J. Phys. Oceanogr.,* **38,** 2379–2413, doi:10.1175/2008JPO3881.1.

Thomson, J., E. A. D'Asaro, M. F. Cronin, W. E. Rogers, R. R. Harcourt, and A. Shcherbina, 2013: Waves and the equilibrium range at Ocean Weather Station P. *J. Geophys. Res. Oceans,* **118,** 5951–5962, doi:10.1002/2013JC008837.

Toba, Y., 1973: Local balance in the air-sea boundary processes. *J. Oceanogr. Soc. Japan,* **29,** 209–220, doi:10.1007/BF02108528.